PNAS RESEARCH ARTICLE | MICROBIOLOGY

A unique bacterial secretion machinery with multiple secretion centers

Liqiang Song[a], John D. Perpich[b], Chenggang Wu[a], Thierry Doan[c], Zuzanna Nowakowska[d], Jan Potempa[b,d], Peter J. Christie[a], Eric Cascales[c,1], Richard J. Lamont[b,1], and Bo Hu[a,1]

Edited by Jorge Galán, Yale University, New Haven, CT; received November 3, 2021; accepted March 22, 2022

The *Porphyromonas gingivalis* type IX secretion system (T9SS) promotes periodontal disease by secreting gingipains and other virulence factors. By in situ cryoelectron tomography, we report that the *P. gingivalis* T9SS consists of 18 PorM dimers arranged as a large, caged ring in the periplasm. Near the outer membrane, PorM dimers interact with a PorKN ring complex of ∼52 nm in diameter. PorMKN translocation complexes of a given T9SS adopt distinct conformations energized by the proton motive force, suggestive of different activation states. At the inner membrane, PorM associates with a cytoplasmic complex that exhibits 12-fold symmetry and requires both PorM and PorL for assembly. Activated motors deliver substrates across the outer membrane via one of eight Sov translocons arranged in a ring. The T9SSs are unique among known secretion systems in bacteria and eukaryotes in their assembly as supramolecular machines composed of apparently independently functioning translocation motors and export pores.

cryoelectron tomography | type IX secretion | protein transport | proton motive force | porphyromonas

Significance

The newly described type IX secretion systems (T9SSs) translocate virulence factors and can mediate specialized gliding motility among bacterial pathogens of the *Fibrobacteres–Chlorobi–Bacterioidetes* superphylum. We visualized the spatial organization of the T9SS in its native context in the *Porphorymonas gingivalis* cell by cryoelectron tomography. The T9SS exhibits distinct symmetries across the bacterial cell envelope: a cytoplasmic complex requiring PorL and PorM for assembly exhibits 12-fold symmetry; a periplasmic complex composed of PorM exhibits 18-fold symmetry and attaches to a PorKN ring near the outer membrane; and eight Sov translocons are arranged with 8-fold symmetry at the cell surface. The T9SS is the largest of the known bacterial secretion systems and evidently arranges as multiple, independently functioning translocation motors.

Bacteria deploy at least 11 different translocation systems to export macromolecules across their cell envelopes (1–3). Of these, the recently discovered type IX secretion systems (T9SSs) carried by many species of the *Fibrobacteres–Chlorobi–Bacteroidetes* (FCB) superphylum play various critical roles in pathogenesis and colonization (4–7). Two bacterial models have emerged for detailed mechanistic and structural analyses of the T9SS. The Por T9SS in *Porphyromonas gingivalis*, a key contributor to human periodontitis and an emerging systemic pathogen, transports various heme-binding proteins and toxins aiding in colonization and invasion of gingival and other tissues (8, 9). The Gld T9SS in *Flavobacterium johnsoniae* secretes adhesins SprB and RemA and dozens of other effector proteins, but also functions as a rotary motor to direct the movement of a surface-bound adhesin along helical tracks, resulting in a form of gliding motility (10, 11). Studies have shown that these T9SSs are large, cell envelope–spanning nanomachines composed of at least 14 essential subunits (Fig. 1*A*) (6, 7). They translocate substrates, exported to the periplasm by the general secretory (Sec) pathway, across the outer membrane (OM). At the cell surface, they release their substrates to the milieu or deliver them to an "attachment complex," which covalently links the substrates to anionic lipopolysaccharides (A-LPSs) for surface display (5, 12).

Three stable subassemblies have been identified through biochemical or single-particle microscopy approaches: 1) An inner membrane (IM) molecular motor composed of the PorL and PorM subunits (13, 14) with structural and functional homologies with the MotAB/PomAB flagellar and ExbBD/TolQR PMF-dependent motors (15–18); 2) a large ∼50-nm ring-shaped complex composed of periplasmic PorN and OM-associated lipoprotein PorK (19, 20); and 3) an OM-spanning translocon, termed Sov or SprA, configured as a 36-strand β-barrel with a central pore of ∼70 Å (21). Despite this progress, it is not yet known how these substructures interact or coordinate their activities, in part because there is no overarching view of the T9SS in the native context of the bacterial cell envelope. Here, we visualized the intact T9SS of *P. gingivalis* by in situ cryoelectron tomography (cryo-ET). Remarkably, the T9SS presents not as a single functional entity, as shown for all known bacterial and eukaryotic protein transport systems, but rather as a composite of apparently independent translocation motors and Sov translocons arranged symmetrically as distinct rings in the cytoplasm, periplasm, and cell surface.

Results and Discussion

The T9SS: A Large, Caged-Ring Structure. *P. gingivalis* cells are small (∼0.5 μm in diameter) and well suited for cryo-ET imaging (Fig. 1*B* and *SI Appendix*, Fig. S1*A*).

Author contributions: R.J.L. and B.H. designed research; L.S., J.D.P., C.W., T.D., Z.N., J.P., E.C., and B.H. performed research; L.S., J.D.P., P.J.C., E.C., R.J.L., and B.H. analyzed data; and P.J.C., E.C., R.J.L., and B.H. wrote the paper.

The authors declare no competing interest.

This article is a PNAS Direct Submission.

[1]To whom correspondence may be addressed. Email: cascales@imm.cnrs.fr, rich.lamont@louisville.edu, or bo.hu@uth.tmc.edu.

This article contains supporting information online at http://www.pnas.org/lookup/suppl/doi:10.1073/pnas.2119907119/-/DCSupplemental.

Published April 26, 2022.

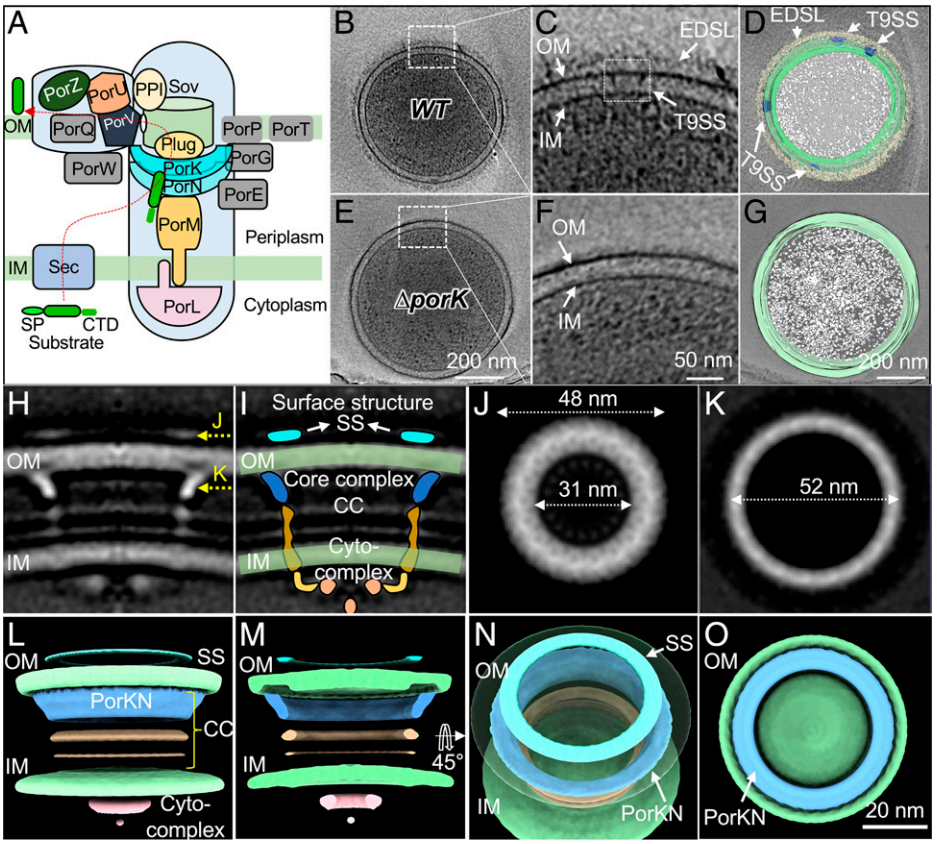

Fig. 1. *P. gingivalis* type IX machine revealed by cryo-ET. (*A*) Schematic representation of the structure and function of the T9SS of *P. gingivalis*. The different subunits are indicated, as well as the putative route for substrate transport (dashed red line). (*B*) A tomographic slice of a wild-type *P. gingivalis* cell. (*C*) Zoomed-in view of *B* showing the OM, IM, EDSL, and a type IX machine (T9SS) embedded in the cell envelope. (*D*) A 3D surface view showing multiple T9SSs embedded in the wild-type *P. gingivalis* cell envelope. (*E*) A tomographic slice of a Δ*porK* mutant of *P. gingivalis* and (*F*) zoomed-in view showing the absence of T9SSs and EDSL. (*G*) A 3D surface view of a *P. gingivalis* Δ*porK* mutant cell. (*H–O*) In situ structure of the *P. gingivalis* T9SS. (*H*) A central section through the longitudinal plane of a global average structure in situ showing T9SS densities in the cell envelope. (*I*) Outline of major features of the T9SS, including the SS, CC, and a cytoplasmic (cyto-) complex. (*J* and *K*) Cross-section views at the position indicated in *H* (yellow arrows) showing the ring-shaped surface structure and periplasmic PorKN complex. To smooth the map, we imposed an 18-fold symmetry. (*L–O*) A 3D surface rendering of the intact T9SS in side, cut-away, 45°, and 90° views.

A typical three-dimensional (3D) reconstruction of a *P. gingivalis* cell revealed the IM and OM, as well as an electron dense surface layer (EDSL), which is known to consist of T9SS substrates attached at the cell surface (Fig. 1 *B–D*) (4). In wild-type (WT) cells, two periplasmic rods attached to the OM and ∼50 nm apart were visualized in side views (Fig. 1 *B–D*, *SI Appendix*, Fig. S1*A*, and Movie S1). In fact, the rods constitute the peripheral edges of a large ring similar in size (∼50 nm) to the previously visualized PorKN rings (19, 20) as shown in tilt and top-down views (*SI Appendix*, Fig. S1 *A* and *B* and Movies S1 and S2). The rods visualized in side view are missing in a strain lacking PorK (Fig. 1 *E* and *F*), which is an essential T9SS subunit (7, 19). The Δ*porK* mutant strain also lacks the EDSL (Fig. 1 *E* and *F*) and fails to secrete T9SS effectors such as the Arg gingipain (Rgp) protease, whereas the *trans*-complemented strain is restored for Rgp secretion (*SI Appendix*, Fig. S2). Similarly, mutants deleted of *porN* are devoid of the EDSL and OM-associated rods and do not secrete Rgp protease (*SI Appendix*, Figs. S1*A* and S2). Previously, it was shown that two IM subunits PorM and PorL with large domains in the periplasm and cytoplasm, respectively (13), are also required for T9SS function, but not for assembly of the PorKN ring (19). Accordingly, here we determined that the Δ*porM* and Δ*porL* mutants lack the EDSL and do not secrete the Rgp effector, but elaborate the OM-associated rod structures (*SI Appendix*, Figs. S1 and S2). Taken together, these findings strongly indicate that the visualized structures correspond to in situ T9SS nanomachines and that the OM-associated rods and rings visualized in side and top-down views correspond to the PorKN ring complexes characterized by single-particle cryoelectron microscopy (cryo-EM) (19) (Fig. 1 *L–O*). The average number of T9SSs visualized by in situ cryo-ET was ∼1.3 per cell with a range of 0 to 4, although this might underestimate the actual number of partially or fully assembled T9SSs per cell (Fig. 1*D*).

To determine the 3D structure of the entire T9SS machine, we imaged over 800 wild-type *P. gingivalis* cells, and picked 694 ring-shaped particles from 516 tomograms (*SI Appendix*, Table S1). By subtomogram averaging, we generated an overall structure of the T9SS at a resolution of ∼32 Å (Fig. 1*H* and *SI Appendix*, Fig. S1C). The T9SS spans the entire cell envelope, with dimensions of ∼57 nm in height and ∼52 nm in width, and consists of three distinct substructures: 1) A surface structure (SS) on the extracellular side of the OM, 2) a periplasmic structure designated here as the core complex (CC), and 3) a cytoplasmic complex (Fig. 1 *H* and *I*). The SS is located ∼6 nm above the OM and below the EDSL and in top-down view presents as a ring with outer and inner diameters of 48 and 31 nm (Fig. 1 *H* and *J*). During initial alignment and without symmetry applied, the SS ring appears to be a featureless ring. We applied 18-fold symmetry to smooth the density; however, upon local refinement and classification (see below), we determined that the SS in fact is composed of eight

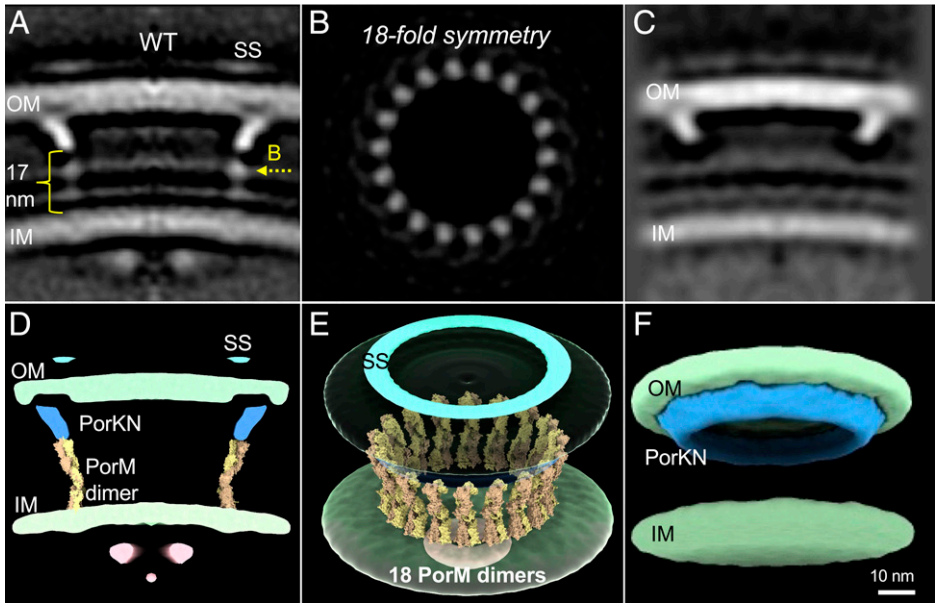

Fig. 2. Molecular architecture of PorM. (*A*) Central section of the native T9SS (WT) showing that the proposed periplasmic arches of PorM span ~17 nm from the IM to the PorKN ring. (*B*) Top-down view of the region denoted in *A* showing 18-fold symmetry of the PorM arches. (*C*) A central section of a global average structure of the T9SS visualized in a Δ*porM* mutant. (*D*) Two PorM dimers (PDB entry 7CMG) docked in the PorM arch density. (*E*) An overall view of T9SS with 18 docked PorM dimers. (*F*) A 3D surface rendering of the Δ*porM* mutant machine showing the presence of the PorKN ring and absence of the PorM arches, cytoplasmic complex, SS, and EDSL.

discontinuous structural units. The CC consists of two parts: 1) The PorKN rods/ring structure (side/top-down views) of ~8 nm in thickness and 52 nm in diameter (Fig. 1 *H* and *K*), and 2) strips of densities presenting in side view as arches of ~17 nm in height that connect the OM-associated PorKN rods to the IM (Figs. 1 *H* and *I* and 2*A*). The cytoplasmic complex consists of a small central knob flanked by two densities when visualized in side view (Fig. 1 *H* and *I*). In 3D surface renderings of the intact T9SS shown at 45° and 90° (top down) angles, ring-shaped architectures of the SS, CC, and cytoplasmic complex are readily evident (Fig. 1 *L*–*O*).

Besides these densities, we detected three layers of density in the periplasm and a fourth between the cell surface and the EDSL (Fig. 1*H* and *SI Appendix*, Fig. S3 *A* and *B*). A 3D map reconstructed by subtomogram averaging of randomly picked regions of the *P. gingivalis* cell envelope established that these four layers are constituents of the cell envelope and are not parts of the T9SS machine (*SI Appendix*, Fig. S3 *C* and *D*). Consequently, the T9SS presents as a large, caged-ring structure that encompasses a central region of the *P. gingivalis* cell envelope whose IM, periplasmic, and OM features are largely intact.

The PorMKN CC. We next focused on solving refined structures of the CC, with emphasis on the side-view arches. Prior studies have shown that PorM has an N-proximal transmembrane domain (TMD) and a large ~480-residue C-terminal region that extends across the periplasm and interacts with the OM-associated PorKN complex (13). By X-ray crystallography, the periplasmic regions of PorM (PorMp) and the *F. johnsoniae* homolog GldM (GldMp) presented as elongated dimers with dimensions 180 Å in length and 50 and 35 Å in cross-sections (22, 23). Through local refinements of periplasmic densities associated with T9SSs in WT cells, we determined that the periplasmic arches correspond to 18 distinct knobs arranged in a ring of 52 nm in diameter when visualized in top-down view (Fig. 2*B* and *SI Appendix*, Tables S1 and S3 and Fig. S4*A*). The Δ*porM* mutant possesses the PorKN ring, but lacks the underlying knobbed ring and the cytoplasmic complex (Fig. 2 *C* and *F*). In consideration of the PorMp and GldMp X-ray structures (22, 23), we propose that the side-view arches and top-down-view knobs correspond to 18 PorM dimers, whose N-proximal regions are anchored in the IM, and C-terminal regions extend through the periplasm to the OM-associated PorKN ring (Fig. 2 *D* and *E*).

The PorMKN complex exhibits two other noteworthy features. First, in the native T9SS, the PorKN ring is 8 nm thick and the PorM arches are 17 nm in length, whereas in the Δ*porM* mutant, the PorKN ring is only 7 nm thick (Fig. 2 *A* and *C* and *SI Appendix*, Fig. S5 *A* and *B*). In the atomic structure, the PorMp dimers are 18 nm in length (23) and composed of four domains, D1–D4, with domain D4 directly interacting with PorN (13, 22). To reconcile these in situ and in vitro findings, the PorKN ring visualized in situ might actually consist of PorK, PorN, and domain D4 of PorM. Alternatively, the interaction between PorM and PorKN might induce a structural change resulting in thickening of the PorKN ring.

Second, in the global averaged map, the PorKN ring forms a 60° angle with respect to the OM (Fig. 3*A*). However, when the PorKN rings were locally refined at the junctions with the PorM arches, we detected three distinct structural classes in which the PorMKN complex forms angles of 90°, 70°, and 50° relative to the OM (Fig. 3*B*). We quantified the PorMKN complexes of each class among the entire set of 12,492 complexes in the 694 imaged T9SSs (18 complexes per T9SS × 694 T9SSs). Among the 12,492 complexes, the class 1 (90°) and class 3 (50°) complexes were more abundant (35.5 and 37.5%, respectively) than the class 2 (70°) complexes (27%) (*SI Appendix*, Fig. S6*A*). Furthermore, among each of the 694 imaged T9SSs, the class 3 complexes dominated with an average of 10 complexes and a range of 3 to 16 per T9SS (*SI Appendix*, Fig. S6*A*). The class 2 structures were least abundant, insofar as ~14% of the T9SSs lacked any class 2 complexes and the bulk of the remaining T9SSs had ≤6. The class 1 complexes had an intermediate distribution with an average of 4 per T9SS and a range of 0 to 10. Importantly, in the absence

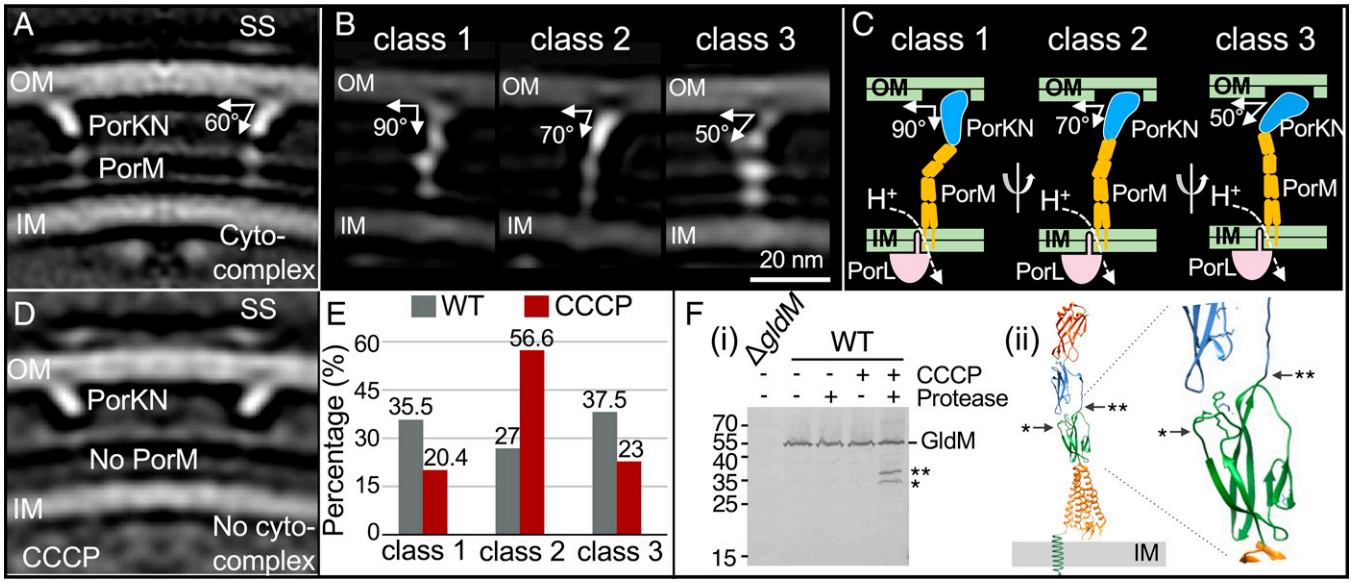

Fig. 3. Proton-motive force-dependent conformational change of the *P. gingivalis* PorM protein and *F. johnsoniae* GldM protein. (*A*) Central section of the native T9SS (WT) showing that the PorKN ring forms an ∼60° angle relative to the OM. (*B*) A 3D classification reveals three distinct classes of PorKNM complex showing that the PorKN ring forms angles of 90° (class 1), 70° (class 2), and 50° (class 3) relative to the OM. (*C*) A proposed model for oscillatory motion of the PorMKN complex. PMF-energy–driven conformational changes of PorM drive the oscillation of PorKN, yielding bend angles of 90° and 50°; the deenergized PorMKN complex is fixed at an angle of 70°. (*D*) A total of 10% of the T9SS machines lack PorM and cytoplasmic complex upon CCCP treatment of WT cells. (*E*) The proportion of each bend-angle class is altered in wild-type cells upon treatment with CCCP. (*F, i*) Limited protease accessibility assay. *F. johnsoniae* wild-type or Δ*gldM* mutant cells were treated with CCCP and spheroplasts were treated with trypsin protease. Proteolytic fragments were visualized by immunostaining of Western blots with anti-GldM antibodies. GldM, full-length protein; * and **, degradation products. Molecular weight markers are indicated on the left. (*F, ii*) Identification of the GldM trypsin cleavage sites. The GldM degradation products were enriched by immunoprecipitation using anti-GldM antibodies and subjected to LS-MS/MS identification. The GldM structure (PDB 6EY4) and magnification are shown, with * and ** denoting cleavage downstream of residues K252 and R322, respectively. For simplification, only a single chain of the GldM dimer is shown.

of *porM*, there was little variation from the 60° global average at the PorKN ring–OM junctions (*SI Appendix*, Fig. S5*D*), indicating that PorM contributes directly to the distinct PorKN–OM junction architectures in WT machines.

Recently, it was shown that PorL and PorM and the *F. johnsoniae* GldL and GldM homologs form structurally similar proton motive force (PMF)-transducing motors (14, 24). Moreover, in the atomic structures, PorMp and GldMp dimers possess distinct bends in the hinge regions between the D1 and D2 or D2 and D3 domain interfaces (14, 21, 22). These finding have led to a model in which PMF-energy transduction regulates the activation states of the PorLM and GldLM translocation motors (14, 25). Upon sensing of the PMF, PorLM and GldLM transduce PMF energy in the form of conformational changes in the periplasmic domains of PorM and GldM as a prerequisite for substrate secretion or gliding motility (25, 26). In this context, we propose that the visualized conformational classes of the PorKMN complexes correspond to different activation states of the motors.

Evidence for PMF-Induced Structural Changes. To further explore whether transduction of PMF energy impacts the conformational status specifically at the PorKN–OM junction, we treated *P. gingivalis* cells with the protonophore carbonyl cyanide m-chlorophenyl hydrazone (CCCP), which disrupts the PMF and inactivates the T9SS (14, 27). Approximately 90% of the visualized T9SSs from CCCP-treated cells possessed all of the structural features of machines from untreated cells, but the remaining 10% lacked PorM arches and the cytoplasmic complex (Fig. 3 *A* and *D*). Among the 90% of T9SSs bearing WT features, we identified significant changes in the relative percentages of classes with distinct PorKN–OM junction angles. Most notably, class 2 structures (bend angle 70°) increased significantly, from 27.0 to 56.6%, upon CCCP treatment. Conversely, the class 1 (bend angle 90°) and class 3 (bend angle 50°) structures decreased from 35.5 to 20.4% and 37.5 to 23%, respectively (Fig. 3*E*). The significant increase in the percentage of class 2 structures in PMF-collapsed cells supports a proposal that this class corresponds to the quiescent or "closed" state of the motor, whereas class 1 and 3 structures represent or activated or "open" states. Why activated motors are represented by bend angles of 90° or 50° could be explained by recent evidence that GldLM in the *F. johnsoniae* T9SS functions as a rotary motor, such that the rotating periplasmic domain of GldM is envisioned to form a large arc as it extends to the PorKN junction (14, 22, 23). Recently, it was also shown that mutations in GldL have different impacts on T9SS activity. Whereas a GldL E49A mutation abolishes both substrate secretion and gliding motility, another mutation, E59A, prevents gliding but does not impact substrate secretion. These findings suggest that GldLM motors exist in a quiescent state and in two activated states, one supporting both gliding motility and substrate secretion and a second only secretion (25).

Whether the *P. gingivalis* Por T9SS rotates is not yet known. If so, a PMF-energized rotating PorM dimer might impose large bend angles at the PorKN junction, and two such activated (class 1 and 3) structural states might have been captured by in situ cryo-ET imaging. By contrast, in the deenergized state, a nonrotating PorM dimer potentially fixes the PorKN junction at the intermediate bend angle represented by class 2 structures. Even if PorM does not rotate, PMF sensing clearly induces large conformational changes in the PorM dimers that are likely mediated through the recently visualized PorLM complex assembled across the IM (24).

Among the small fraction (∼10%) of T9SSs from CCCP-treated cells that lacked the PorM arches and cytoplasmic complexes (Fig. 3*D*), the bend angle of the PorKN–OM junction approximates that observed for Δ*porM* mutant machines.

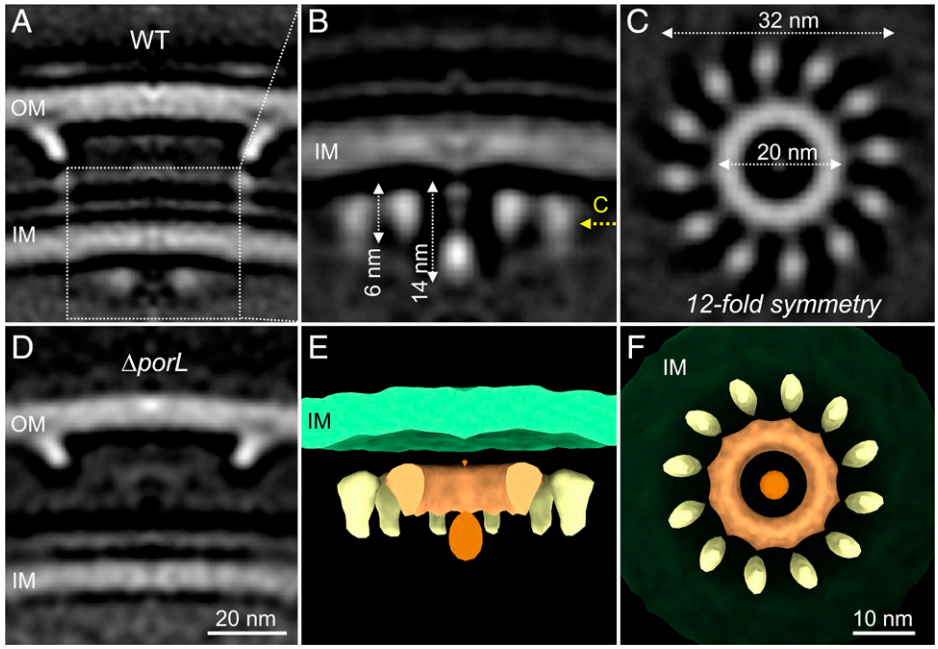

Fig. 4. Architecture of the cytoplasmic complex. (*A*) Unrefined structure. (*B*) The cytoplasmic complex boxed in *A* was locally refined. A central knobbed cylinder extends ~14 nm into the cytoplasm from the IM, and flanking densities extend ~6 nm. (*C*) Bottom-up view of the region denoted in *B* showing 12-fold symmetry of the outer spoked ring of ~32 nm and a continuous inner ring of ~20 nm. (*D*) A central section of a global average structure of the T9SS visualized in a Δ*porL* mutant showing the presence of the PorKN ring and absence of the PorM periplasmic arches, cytoplasmic complex, SS, and EDSL. (*E* and *F*) A 3D rendering of the cytoplasmic complex shown in side and bottom-up views.

CCCP-induced disengagement of the PorM arches therefore phenocopies the Δ*porM* mutation with respect to the overall PorKN ring architecture. Importantly, however, this subpopulation of CCCP-deenergized T9SSs retains the SSs that are lacking in the Δ*porM* or Δ*porL* mutant machines (Figs. 2*C* and 4*D*). In a small fraction of T9SSs deenergized by collapse of the PMF, PorM, and PorL thus appear to disengage from the PorKN ring without destabilization of the previously docked SS.

We sought to gain further biochemical evidence for PMF-mediated activation of T9SSs, and to this end we capitalized on the availability of antibodies to assay for energy-mediated conformational changes in the PorM and PorN homologs, GldM and GldN, in *F. johnsoniae* cells. Reminiscent of previous findings for the PMF-responsive energy transducer TonB (28), trypsin treatments of spheroplasts derived from CCCP-untreated or -treated cells yielded different GldM protease cleavage patterns (Fig. 3*F*). In the absence of CCCP treatment, GldM remained intact upon exposure to trypsin, whereas CCCP treatment resulted in the generation of two GldM cleavage products. By liquid chromatography with tandem mass spectrometry (LC-MS/MS), we determined that both cleavage sites (downstream residues Lys252 and Arg322, respectively) reside within the linker region between domains D2 and D3 (Fig. 3*F*). We were unable to assess the effect of PMF-energy depletion on the conformational status of GldN, as the GldN trypsin cleavage patterns were unaltered regardless of prior treatment of cells with CCCP (*SI Appendix*, Fig. S7). Overall, these data confirm earlier predictions that GldLM transduces IM energy from the PMF in the form of a conformational change(s) in the periplasmic arms of GldM to activate the T9SS for transport or gliding motility (22). In view of the structural homology of GldM and PorM, we suggest that PMF sensing similarly induces conformational changes in the PorM translocation motor. With respect to the PMF-driven conformational changes we observed here for individual PorKMN complexes, it is interesting to note that complexes of a given bend-angle class tend to spatially cluster within each T9SS (*SI Appendix*, Fig. S6 *A* and *B*). This clustering could imply that adjacent complexes are coordinately activated in response to PMF-energy sensing.

Refinement of the Cytoplasmic Complex. To better understand the structural basis for energy transduction, we locally refined the cytoplasmic complex (Fig. 4 *A*–*C* and *SI Appendix*, Fig. S4*B*). Three distinct densities were evident: 1) A central knobbed cylinder projecting ~14 nm from the IM into the cytoplasm, 2) a flanking ring of ~6 nm in thickness and ~20 nm in diameter, and 3) a spoked ring of ~32 nm in diameter with 12-fold symmetry (Fig. 4 *B* and *C* and *SI Appendix*, Fig. S4*B*). PorL and PorM are the only essential T9SS proteins identified to date with cytoplasmic domains (Fig. 1*A*). Indeed, the Δ*porL* and Δ*porM* mutant machines lack the periplasmic arches and cytoplasmic densities, showing a codependence on PorL and PorM for assembly of these structures (Figs. 2*C* and 4*D*). PorM spans the IM once and its ~9-residue, N-terminal cytoplasmic domain is unlikely to contribute detectable density. By contrast, PorL has two N-terminal transmembrane helices (TMHs) and its large (~230 residue) C-terminal domain resides in the cytoplasm (24). Recently, the 3D structures of the PorLM and GldLM complexes were shown to consist of the 10 TMHs from five PorL subunits arranged in a ring surrounding the two TM helices of the PorM dimer (14, 24). Thus, the five cytoplasmic domains of PorL associated with the recently visualized PorLM complex (24) might contribute to one or more of the cytoplasmic densities detected by in situ cryo-ET.

The PorM dimers are in close juxtaposition with the outermost cytoplasmic knobs, suggesting the possibility that they are composed of PorL pentamers (*SI Appendix*, Fig. S4*B*, classes *e*–*h*). If so, it is necessary to account for the 18- vs. 12-fold symmetry mismatch that exists between the PorM arches and putative PorL knobs. Conceivably, a PorM dimer engages

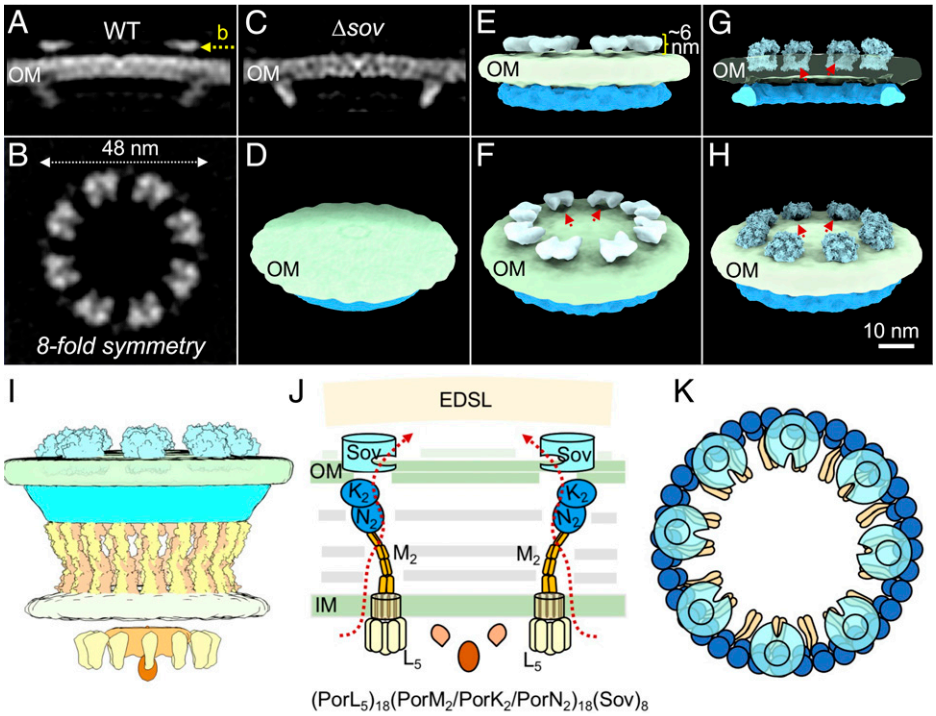

Fig. 5. Organization of secretion pore (Sov) at the OM. (*A* and *B*) Central-section and top-down views of the locally refined surface structure showing eight distinct densities arranged in a ring of 48 nm in diameter. (*C*) A central section through longitudinal plane of a global average structure of a Δ*sov* mutant machine and 3D surface rendering (*D*) showing that the surface densities are absent. (*E* and *F*) A 3D surface rendering of the putative translocons shown in different views. Arrows in *F* denote lateral pores. (*G* and *H*) Eight SprA molecules (PDB entry 6H3J) docked into the surface densities. Arrows denote lateral pores facing the center of the T9SS complex. (*I*) A side view of the entire of T9SS machine showing cytoplasmic, periplasmic, and surface substructures. (*J* and *K*) Schematic of the *P. gingivalis* T9SS multiport export apparatus, with major machine subunits and postulated routes of substrate translocation shown. Substrates cross the IM through the Sec system, are recruited by the PorLMNK translocation motor, enter a gap in the inner leaflet of the OM and then the Sov translocon, and exit Sov through lateral pores for release to the milieu or docking onto the cell surface via the attachment complex. The proposed stoichiometry of the major machine subunits is shown.

stably with the PorL pentamer only when activated, for example, upon sensing of bound substrate in the periplasm. Such a model of substrate-induced PorLM engagement might allow for one PorL pentamer to interact with and energize more than one spatially juxtaposed PorM dimer, which would account for our observation that PorKMN complexes of a given structural class, or activation state, tend to spatially cluster within each T9SS (*SI Appendix*, Fig. S6 *A* and *B*). It is important to note, however, that PorL's cytoplasmic domain is disordered when purified and analyzed by single-particle cryo-EM (14). If this domain is also too flexible for detection by in situ cryo-ET, the visualized densities might instead correspond to other Por components. One candidate is PorX, the response regulator of the PorXY two-component system that was shown to interact with PorL (29), but further studies are needed to define subunit contributions to the observed cytoplasmic densities.

The SS. Finally, we refined the structure of the SS visualized initially as an extracellular ring (Fig. 1*J*). Strikingly, the SS presents as eight distinct densities of 8 nm in diameter arranged in a ring of ∼48 nm in diameter (Fig. 5 *A* and *B* and *SI Appendix*, Fig. S4*C*). Each of the eight densities has a lateral pore near the OM that faces the center of the T9SS supramolecular complex (Fig. 5 *E* and *F*). The overall size and presence of a lateral pore are highly reminiscent of the 267-kDa SprA/Sov translocon solved at ∼3.5 Å by single-particle cryo-EM (20). This cryo-EM structure docks well on the SS densities (Fig. 5 *G* and *H* and *SI Appendix*, Fig. S8 *A* and *B*). Moreover, a strain deleted of Sov retained all features of the T9SS except for the SS; this strain also lacked the EDSL and failed to secrete Rgp protease (Fig. 5 *C* and *D* and *SI Appendix*, Figs. S1 and S2). Considering the size of Sov protein, we propose that the SS densities are largely composed of Sov, with potential contributions from other components, e.g., the PorV shuttle protein (30). In the cryo-EM structure, the location of detergent associated with the translocon was used to define the likely plane of the OM, giving rise to the proposal that the β-barrel extends ∼2 nm above the OM and an extracellular cap projects an additional 5 nm (21). In line with those findings, the SS densities project ∼6 to 7 nm above the OM (Fig. 5*E*). Interestingly, beneath each of the Sov densities, the OM is missing its inner leaflet (Fig. 5*A* and *SI Appendix*, Fig. S8*A*). This gap or hole might be a point of entry for substrates, delivered by the PorLMKN translocation motor, into the Sov translocon. The importance of the translocation motor–Sov contact for a stable association of translocons with the T9SS is underscored by the fact that deletions of any of the translocation motor subunits abolished detectable Sov surface densities (Figs. 2*C* and 4*D*). Intriguingly, despite numerous attempts, no studies have yet shown a direct interaction between the PorL/M/K/N proteins and the Sov translocon. Recently, however, a protein interactome analysis identified PorW as a mutually interacting partner of Sov and the PorKN ring. PorW thus appears to constitute a critical link between these subassemblies (31).

Summary. We have shown that the *P. gingivalis* T9SS assembles as a large supramolecular machine composed of a cytoplasmic complex with 12-fold symmetry, a periplasmic complex with 18-fold symmetry, and a surface structure consisting of eight symmetrically arranged putative pores (Fig. 5*I*). Taken

together with previous findings, we propose a working model in which the major machine subunits assemble with an overall stoichiometry of $(PorL_5/PorM_2/PorK_2/PorN_2)_{18}(Sov)_8$ (Fig. 5*J*). Observed differences in the bend angles at PorMKN–OM junctions (Fig. 3*B*), coupled with the absence of a discernible central channel (Fig. 2*A* and *SI Appendix*, Fig. S3*A*), support our model that the T9SS is a multiport export apparatus composed of independently—but coordinately—functioning IM energy sensors, periplasmic translocation motors, and OM translocons (Fig. 4 *J* and *K* and Movie S3). This proposed architecture and mechanism of action strikingly contrast with other known dedicated protein translocation systems functioning in bacteria (1–3, 32, 33) (*SI Appendix*, Fig. S9). Deciphering the molecular and structural details underlying IM energy activation, substrate recruitment, and OM export remain as major challenges for future research on this unique family of bacterial transporters.

Materials and Methods

***P. gingivalis* Growth and Mutant Constructions.** *P. gingivalis* American Type Culture Collection (ATCC) 33277 (33277) and W83 and their isogenic mutants were cultured anaerobically at 37 °C in trypticase soy broth (TSB) supplemented with 1 mg ml^{-1} yeast extract, 5 μg ml^{-1} hemin, and 1 μg ml^{-1} menadione. When appropriate, erythromycin (10 μg ml^{-1}) was added to the medium.

The PCR fusion technique was utilized to generate allelic exchange mutants Δ*porK*, Δ*porL*, Δ*porM*, Δ*porN*, (all ATCC 33277) and Δ*sov* (W83) as described previously (34). Upstream and downstream fragments of each gene were amplified by PCR and fused to *ermF* using the primers listed in *SI Appendix*, Table S2. Constructs were confirmed by sequencing and introduced into *P. gingivalis* by electroporation, and mutant strains were selected on TSB plates containing erythromycin. Loss of mRNA from the target gene without disruption of expression of the other genes in the operon (*por* operon) was confirmed by RT-PCR (*SI Appendix*, Fig. S10) using the primers listed in *SI Appendix*, Table S2.

For complementation of *porK* in *P. gingivalis* ATCC 33277, a 500-bp sequence upstream of PGN_1678 containing the promoter region was fused to the coding region of *porK* using PCR fusion and the primers listed in *SI Appendix*, Table S2. The resulting PCR product was confirmed by sequencing and cloned into the pT-COW vector to create pT-COW-*porK*. The plasmid was transformed into chemically competent *Escherichia coli* (strain S17-1) and selected using ampicillin. The plasmid was transferred into *P. gingivalis* Δ*porK* via conjugation with *E. coli* (35, 36), and transconjugants were selected with gentamicin (50 μg ml^{-1}) and tetracycline.

F. johnsoniae CJ1827 (UW101 *rpsL*, Str^R) and its Δ*gldM* isogenic mutant have been previously described (37). *F. johnsoniae* strains were grown in casitone-yeast extract (CYE) medium (10 g L^{-1} casitone, 5 g L^{-1} yeast extract, 8 mM $MgSO_4$, 10 mM Tris·HCl pH 7.6) at 28 °C with agitation. The proton motive force uncoupler CCCP (Sigma-Aldrich) was solubilized in ethanol and added in the culture 30 min prior to cell harvesting, at the final concentration of 10 μM.

Spheroplasting and Limited Proteolysis. *F. johnsoniae* UW101 cells were grown in 5 mL of CYE medium to an $A_{600} = 0.8$, harvested by centrifugation, and resuspended in 100 μL of 20 mM Tris·HCl pH 8.0, 20% sucrose, 1 mM EDTA (ethylenediaminetetraacetic acid), and 100 μg ml^{-1} of lysozyme. After a 30-min incubation at room temperature (20 °C), 100 μL of ice-cold sterile water was added, and the mixture was carefully mixed by three inversions. A total of 50 μL of the spheroplast suspension was treated with trypsin (100 μg ml^{-1}). After 5 min on ice, 17 μL of boiling 4× Laemmli loading buffer was added and immediately vortexed and boiled for 5 min prior to sodium dodecyl sulfate–polyacrylamide gel electrophoresis (SDS-PAGE).

Immunoprecipitation and LC-MS/MS Analyses. *F. johnsoniae* spheroplasts obtained from a 50-mL culture treated with 10 μM CCCP were prepared and subjected to limited proteolysis using trypsin. Proteolysed spheroplasts were resuspended in 1 mL of CelLytic (Sigma-Aldrich) in the presence of aprotinin (Sigma-Aldrich), and incubated for 30 min on a wheel at room temperature. Unsolubilized material was discarded by centrifugation for 10 min at 20,000 × *g* and subjected to immunoprecipitation using anti-GldM antibodies bound to Protein A Sepharose CL-4B (GE Healthcare). After 2 h of incubation at room temperature on a wheel, the beads were washed three times with CelLytic B, resuspended in Laemmli loading buffer, and subjected to SDS-PAGE and InstantBlue staining (Expedeon). Bands corresponding to the proteolytic products were cut; washed with 100 mM acetonitrile/ammonium bicarbonate, pH 7.5; reduced by 10 mM dithiothreitol in 100 mM ammonium bicarbonate, pH 7.5; alkylated by 55 mM iodoacetamide in 100 mM ammonium bicarbonate, pH 7.5; and then digested overnight at 37 °C with 10 ng/μL^{-1} of trypsin/Lys-C mix from *Pseudomonas aeruginosa* (Promega) in 25 mM ammonium bicarbonate, pH 7.5, 0.025% (vol/vol) proteaseMAX surfactant (Promega). Tryptic peptides were extracted from gel bands by 0.1% (vol/vol) trifluoroacetic acid, 0.01% (vol/vol) proteaseMAX, 50% (vol/vol) acetonitrile, and dried by speed vacuum. Samples solubilized in 0.05% (vol/vol) trifluoroacetic acid, 2% (vol/vol) acetonitrile were analyzed on a ESI-Q-Exactive Plus (Thermo Fisher) mass spectrometer coupled to a nanoliquid chromatography (Ultimate 3000, Dionex). Peptides were eluted from a C18 column (Acclaim PepMap RSLC, 75 μm × 150 mm, 2 μm, 100 Å, Dionex) by a 6 to 40% linear gradient of mobile phase B (0.1% (vol/vol) formic acid/80% (vol/vol) acetonitrile) in mobile phase A (0.1% (vol/vol) formic acid) for 52 min. The peptides were detected in the mass spectrometer in a positive ion mode using a top 10 data-dependent workflow. A single full scan acquisition in the Orbitrap at a resolution of 70,000 in a 350 to 1,900 *m/z* range was followed by a fragmentation MS/MS step, at a resolution of 17,500, of the 10 top ions, in the higher energy collisional dissociation cell set at 27 eV. The spectra were processed by Proteome Discoverer software (Thermo Fisher, version 2.1.0.81) using the Sequest HT algorithm with the following search parameters: *F. johnsoniae* UW101 GldM protein (GeneBank identifier [GI]: 58531935); trypsin enzyme (maximum 2 missed cleavages); fixed modification: carbamidomethyl (Cys); variable modification: oxidation (Met); mass values specific for monoisotopic; precursor mass tolerance: ±10 ppm; and fragment mass tolerance: ±0.02 Da.

Preparation of Frozen-Hydrated Specimens. Strains grown anaerobically at 37 °C were harvested in the late log phase by centrifugation at 9,000 × *g*. The pellet was resuspended in phosphate-buffered saline (PBS). To prepare CCCP-treated wild-type cells, CCCP was added to a final concentration of 20 μM and incubated for 20 min and then mixed with 10-nm diameter colloidal gold beads (used as fiducial markers in image alignment) and deposited onto freshly glow-discharged, holey carbon grids for 1 min. The grids were then blotted with filter paper and rapidly frozen in liquid ethane, using a gravity-driven plunger apparatus as previously described (33).

Cryo-ET Data Collection and 3D Reconstructions. Frozen-hydrated specimens were imaged at −170 °C using a Polara G2 electron microscope (FEI Company) equipped with a field emission gun and a direct detection device (Gatan K2 Summit). The microscope was operated at 300 kV with a magnification of ×9,400, resulting in an effective pixel size of 4.5 Å at the specimen level. We used SerialEM (38) to collect low-dose, single-axis tilt series with dose fractionation mode at about 8 μm defocus. Tilt series were collected from −51° to 51° with an increment of 3° and a cumulative dose of ∼70 $e^-/Å^2$ distributed over 35 stacks. Each stack contains approximately eight images. We used Tomoauto (39) to facilitate data processing, which includes drift correction of dose-fractionated data using Motioncorr (40) and assembly of corrected sums into tilt series, automatic fiducial seed model generation, alignment, and contrast transfer function correction of tilt series by IMOD (41) and weighted back projection (WBP) reconstruction of tilt series into tomograms using Tomo3D (42). Each tomographic reconstruction is 3,710 × 3,838 × 1,600 pixels and ∼1.30 Gb in size. In total, 4,227 tomographic reconstructions from six different strains were generated.

Subtomogram Averaging and Correspondence Analysis. We used tomographic package I3 for subtomogram analysis as described previously (43). A total of 2,936 type IX secretion machines (400 × 400 × 400 voxels) were visually identified and then extracted from 1,947 tomographic reconstructions. Two of the three Euler angles of each secretion machine were estimated based on the orientation of each particle in the cell envelope. To accelerate image analysis, 4 × 4 × 4 binned subtomograms (100 × 100 × 100 voxels) were used for initial alignment. The alignment proceeds iteratively with each iteration consisting of three parts in which references and classification masks are generated, subtomograms are aligned and classified, and finally class averages are aligned to each

other. After multiple cycles of alignment and classification for 4 × 4 × 4 binned subtomograms, we used 2 × 2 × 2 binned subtomograms for refinement. The initial alignments were carried out without symmetry imposed. To determine the symmetry of the SS, CC, and cytoplasmic complex, after the initial alignments of the intact machine, the rotation centers of the subvolumes were moved to the corresponding centers of SS, CC, and cytoplasmic complex, respectively, and masks were applied to include the SS, CC, or cytoplasmic complex. Once the symmetries were determined through classification, one of the classes was used as reference to align other classes and the corresponding symmetry was applied to the final refinements. Fourier shell correlation (FSC) between the two independent reconstructions was used to estimate the resolution of the averaged structures.

Visualization and Molecular Modeling. We used IMOD to visualize the maps. IMOD and EMAN2 (41, 44) were used to generate 3D surface renderings of *P. gingivalis* cells and University of California, San Francisco ChimeraX (http://www.rbvi.ucsf.edu/chimerax) to visualize subtomogram averages in 3D and molecular modeling. Each of 18 PorM dimer structures (Protein Data Bank [PDB] 7CMG) was manually fitted onto each of the 18 arches of densities. We docked the Sov homolog SprA (PDB 6H3J) into the eight pore densities on the cell surface.

Quantification and Statistical Analyses. Quantification and statistical analyses are integral parts of the algorithms and software used in our high throughput cryoelectron tomography pipeline. In particular, massive data enabled us to use multivariate statistical analysis and classification (which are implemented in tomographic package I3) for processing and interpretation of the subtomograms of T9SS extracted from *P. gingivalis* cell reconstructions.

Data Availability. Density maps data that support the T9SS structures determined by cryoelectron tomography data have been deposited in Electron Microscopy Data Bank (EMD-24227 (intact machine: PorM arches/ring), EMD-24228 (cytoplasmic complex), and EMD-24229 (Sov SS). All other study data are included in the article and/or supporting information.

ACKNOWLEDGMENTS. We are grateful to members of the B.H., R.J.L., and E.C. laboratories for critical discussions. We are grateful to Dr. William Margolin for suggestions and critiques of the manuscript, Pascal Mansuelle (Institut de Microbiologie de la Méditerranée proteomic platform, Marseille) for mass spectrometry analyses, and Mark McBride (University of Wisconsin, Milwaukee) for anti-GldM and -GldN antibodies. B.H. was supported in part by McGovern Medical School startup funds, the Welch Foundation (AU-1953-20180324), and NIH 1R35GM138301. R.J.L. was supported by NIH grants DE011111, DE012505, and DE023193. E.C. was supported by the Fondation Bettencourt-Schueller, the Excellence Initiative of Aix-Marseille University-A*MIDEX grant A-M-AAP-ID-17-33-170301-07.22, and Agence Nationale de la Recherche grant ANR-20-CE11-0011. P.J.C. was supported by NIH grants R01GM48476 and R35GM131892. C.W. was supported by NIH grant DE030895. We thank the UTHealth CryoEM Core Facility for use of their microscopes and facilities.

Author affiliations: [a]Department of Microbiology and Molecular Genetics, McGovern Medical School, Houston, TX 77030; [b]Department of Oral Immunology and Infectious Diseases, University of Louisville, Louisville, KY 40292; [c]Laboratoire d'Ingénierie des Systèmes Macromoléculaires, Institut de Microbiologie, Bioénergies et Biotechnologie, CNRS UMR7255, Aix-Marseille Université, Marseille, 13402 France; and [d]Department of Microbiology, Faculty of Biochemistry, Biophysics, and Biotechnology, Jagiellonian University, Krakow, 30-387 Poland

1. J. E. Galán, G. Waksman, Protein-injection machines in bacteria. *Cell* **172**, 1306–1318 (2018).
2. P. J. Christie, The rich tapestry of bacterial protein translocation systems. *Protein J.* **38**, 389–408 (2019).
3. D. D. Majewski, L. J. Worrall, N. C. Strynadka, Secretins revealed: Structural insights into the giant gated outer membrane portals of bacteria. *Curr. Opin. Struct. Biol.* **51**, 61–72 (2018).
4. P. D. Veith, M. D. Glew, D. G. Gorasia, E. C. Reynolds, Type IX secretion: The generation of bacterial cell surface coatings involved in virulence, gliding motility and the degradation of complex biopolymers. *Mol. Microbiol.* **106**, 35–53 (2017).
5. A. M. Lasica, M. Ksiazek, M. Madej, J. Potempa, The type IX secretion system (T9SS): Highlights and recent insights into its structure and function. *Front. Cell. Infect. Microbiol.* **7**, 215 (2017).
6. M. J. McBride, Bacteroidetes gliding motility and the type IX secretion system. *Microbiol. Spectr.* **7**, 7.1.5 (2019).
7. K. Sato *et al.*, A protein secretion system linked to bacteroidete gliding motility and pathogenesis. *Proc. Natl. Acad. Sci. U.S.A.* **107**, 276–281 (2010).
8. N. M. O'Brien-Simpson *et al.*, Role of RgpA, RgpB, and Kgp proteinases in virulence of *Porphyromonas gingivalis* W50 in a murine lesion model. *Infect. Immun.* **69**, 7527–7534 (2001).
9. K. Nakayama, *Porphyromonas gingivalis* and related bacteria: From colonial pigmentation to the type IX secretion system and gliding motility. *J. Periodontal Res.* **50**, 1–8 (2015).
10. A. Shrivastava, T. Roland, H. C. Berg, The screw-like movement of a gliding bacterium is powered by spiral motion of cell-surface adhesins. *Biophys. J.* **111**, 1008–1013 (2016).
11. D. Nakane, K. Sato, H. Wada, M. J. McBride, K. Nakayama, Helical flow of surface protein required for bacterial gliding motility. *Proc. Natl. Acad. Sci. U.S.A.* **110**, 11145–11150 (2013).
12. P. D. Veith *et al.*, Protein substrates of a novel secretion system are numerous in the Bacteroidetes phylum and have in common a cleavable C-terminal secretion signal, extensive post-translational modification, and cell-surface attachment. *J. Proteome Res.* **12**, 4449–4461 (2013).
13. M. S. Vincent *et al.*, Characterization of the *Porphyromonas gingivalis* type IX secretion trans-envelope PorKLMNP core complex. *J. Biol. Chem.* **292**, 3252–3261 (2017).
14. R. Hennell James *et al.*, Structure and mechanism of the proton-driven motor that powers type 9 secretion and gliding motility. *Nat. Microbiol.* **6**, 221–233 (2021).
15. M. Santiveri *et al.*, Structure and function of stator units of the bacterial flagellar motor. *Cell* **183**, 244–257.e16 (2020).
16. J. C. Deme *et al.*, Structures of the stator complex that drives rotation of the bacterial flagellum. *Nat. Microbiol.* **5**, 1553–1564 (2020).
17. H. Celia *et al.*, Cryo-EM structure of the bacterial Ton motor subcomplex ExbB-ExbD provides information on structure and stoichiometry. *Commun. Biol.* **2**, 358 (2019).
18. S. Zhu *et al.*, *In situ* structure of the *Vibrio* polar flagellum reveals a distinct outer membrane complex and its specific interaction with the stator. *J. Bacteriol.* **202**, e00592-19 (2020).
19. D. G. Gorasia *et al.*, Structural insights into the PorK and PorN components of the *Porphyromonas gingivalis* type IX secretion system. *PLoS Pathog.* **12**, e1005820 (2016).
20. D. G. Gorasia *et al.*, *In situ* structure and organisation of the type IX secretion system. *bioRxiv* [Preprint] (2020). https://doi.org/10.1101/2020.05.13.094771. Accessed 6 January 2020.
21. F. Lauber, J. C. Deme, S. M. Lea, B. C. Berks, Type 9 secretion system structures reveal a new protein transport mechanism. *Nature* **564**, 77–82 (2018).
22. P. Leone *et al.*, Type IX secretion system PorM and gliding machinery GldM form arches spanning the periplasmic space. *Nat. Commun.* **9**, 429 (2018).
23. K. Sato, K. Okada, K. Nakayama, K. Imada, PorM, a core component of bacterial type IX secretion system, forms a dimer with a unique kinked-rod shape. *Biochem. Biophys. Res. Commun.* **532**, 114–119 (2020).
24. R. H. James *et al.*, Structures of the type IX secretion/gliding motility motor from across the phylum *Bacteroidetes*. bioRxiv [Preprint] (2022). https://www.biorxiv.org/content/10.1101/2022.01.28.478170v1. Accessed 2 January 2022.
25. M. S. Vincent *et al.*, Dynamic proton-dependent motors power type IX secretion and gliding motility in *Flavobacterium*. *PLoS Biol.* **20**, e3001443 (2022).
26. P. D. Veith *et al.*, The type IX secretion system and its role in bacterial function and pathogenesis. *J. Dent. Res.* **101**, 374–383 (2022).
27. J. L. Pate, L. Y. E. Chang, Evidence that gliding motility in prokaryotic cells is driven by rotary assemblies in the cell envelopes. *Curr. Microbiol.* **2**, 59–64 (1979).
28. R. A. Larsen, Assessing energy-dependent protein conformational changes in the TonB system. *Methods Mol. Biol.* **1615**, 277–287 (2017).
29. M. S. Vincent, E. Durand, E. Cascales, The PorX response regulator of the *Porphyromonas gingivalis* PorXY two-component system does not directly regulate the type IX secretion genes but binds the PorL subunit. *Front. Cell. Infect. Microbiol.* **6**, 96 (2016).
30. M. D. Glew *et al.*, PorV is an outer membrane shuttle protein for the type IX secretion system. *Sci. Rep.* **7**, 8790 (2017).
31. D. G. Gorasia *et al.*, Protein interactome analysis of the type IX secretion system identifies PorW as the missing link between the PorK/N ring complex and the Sov translocon. *Microbiol. Spectr.* **10**, e0160221 (2022).
32. B. Hu, M. Lara-Tejero, Q. Kong, J. E. Galán, J. Liu, *In situ* molecular architecture of the *Salmonella* Type III secretion machine. *Cell* **168**, 1065–1074.e10 (2017).
33. B. Hu, P. Khara, P. J. Christie, Structural bases for F plasmid conjugation and F pilus biogenesis in *Escherichia coli*. *Proc. Natl. Acad. Sci. U.S.A.* **116**, 14222–14227 (2019).
34. M. R. Simionato *et al.*, *Porphyromonas gingivalis* genes involved in community development with *Streptococcus gordonii*. *Infect. Immun.* **74**, 6419–6428 (2006).
35. C. E. James *et al.*, LuxS involvement in the regulation of genes coding for hemin and iron acquisition systems in *Porphyromonas gingivalis*. *Infect. Immun.* **74**, 3834–3844 (2006).
36. Y. Park, R. J. Lamont, Contact-dependent protein secretion in *Porphyromonas gingivalis*. *Infect. Immun.* **66**, 4777–4782 (1998).
37. A. Shrivastava, J. J. Johnston, J. M. van Baaren, M. J. McBride, *Flavobacterium johnsoniae* GldK, GldL, GldM, and SprA are required for secretion of the cell surface gliding motility adhesins SprB and RemA. *J. Bacteriol.* **195**, 3201–3212 (2013).
38. D. N. Mastronarde, Automated electron microscope tomography using robust prediction of specimen movements. *J. Struct. Biol.* **152**, 36–51 (2005).
39. D. R. Morado, B. Hu, J. Liu, Using Tomoauto: A protocol for high-throughput automated cryo-electron tomography. *J. Vis. Exp.* **107**, e53608 (2016).
40. X. Li *et al.*, Electron counting and beam-induced motion correction enable near-atomic-resolution single-particle cryo-EM. *Nat. Methods* **10**, 584–590 (2013).
41. J. R. Kremer, D. N. Mastronarde, J. R. McIntosh, Computer visualization of three-dimensional image data using IMOD. *J. Struct. Biol.* **116**, 71–76 (1996).
42. J. I. Agulleiro, J. J. Fernandez, Tomo3D 2.0–Exploitation of advanced vector extensions (AVX) for 3D reconstruction. *J. Struct. Biol.* **189**, 147–152 (2015).
43. H. Winkler, 3D reconstruction and processing of volumetric data in cryo-electron tomography. *J. Struct. Biol.* **157**, 126–137 (2007).
44. M. Chen *et al.*, A complete data processing workflow for cryo-ET and subtomogram averaging. *Nat. Methods* **16**, 1161–1168 (2019).